RSC Advances

PAPER

View Article Online
View Journal | View Issue

Check for updates

Cite this: *RSC Adv.*, 2025, **15**, 43955

Stark effects of the fluorescence spectra in InP core and InP/ZnSe core/shell quantum dots under an external electric field

Ning Du * and Hongshan Chen

Investigating the optical response of quantum dots subjected to an external electric field offers key insights into their suitability for nanoelectronic device integration. In this study, we employ first-principles calculations to elucidate the Stark effect in both InP core and InP/ZnSe core/shell quantum dots. Our analysis reveals three characteristic Stark shift behaviors, including quadratic, linear, and hybrid quadratic-linear responses, where each is directly linked to the evolution of the excitonic dipole moment, reflecting the intrinsic electron–hole separation (D_{0i}, where $i = x, y, z$) in the absence of an applied field. Calculated electron densities for excited states demonstrate that spectral energy ΔE increases as $|D_i|$ decreases under an external electric field, reaching a maximum when $|D_i|$ approaches zero. For all the QDs examined, D_{0x} is approximately zero, so an applied field along the x-direction consistently enlarges $|D_x|$, resulting in a red shift. In contrast, the spectral response along the y or z axes depends on the alignment of the field orientation relative to D_{0i}: fields aligning with the electron–hole vector enhance separation (red shift), while opposing fields reduce it (blue shift). The magnitude of $|D_{0i}|$ is primarily determined by core/shell electronic structure: small-core $(InP)_{10}(ZnSe)_{67}$ exhibits quasi-type II behavior with large $|D_{0z}|$, while larger-core $(InP)_{27}(ZnSe)_{50}$ and pure $(InP)_{77}$ show type-I-like localization with small $|D_{0i}|$. These findings indicate that the Stark shift characteristics of InP/ZnSe QDs can be tailored by adjusting the thickness of the core or shell layer of QDs.

Received 25th August 2025
Accepted 31st October 2025

DOI: 10.1039/d5ra06323j

rsc.li/rsc-advances

Open Access Article. Published on 12 November 2025. Downloaded on 12/24/2025 5:45:51 PM.
This article is licensed under a Creative Commons Attribution-NonCommercial 3.0 Unported Licence.

1 Introduction

Quantum dots (QDs) are nanoscale semiconductor crystals characterized by discrete energy levels and size-dependent optical properties. When subjected to an external electric field or photon excitation, QDs emit light at tunable frequencies by varying their sizes, a phenomenon commonly referred to as the quantum confinement effect. Through precise control of both particle size and chemical composition, the emission spectra of QDs can span the entire visible range, enabling dynamic modulation of their optical output. This tunability, alongside features such as broad absorption, narrow and intense emission, high photostability, and superior color purity, has propelled QDs to the forefront of research in optoelectronics, bioimaging, and energy technologies. Among the wide range of available QD materials, cadmium-based systems have reached a high level of technological maturity, and Cd-based quantum dot light-emitting diodes (QLEDs) now fulfill commercial display requirements.[1,2] However, concerns over toxicity and environmental impact restrict their widespread deployment. Indium phosphide (InP) QDs, as a cadmium-free alternative, possess a Bohr radius near 10 nm and exhibit emission that can be tuned throughout the visible spectrum by controlling particle size. Substantial advances in the synthesis and surface engineering of InP QDs have led to marked improvements in their performance, rendering them increasingly attractive for applications in displays.[3–5] For instance, the external quantum efficiency (EQE) of red and green QLED reached 22.56%,[6] and 16.3%,[7] respectively.

Although blue-emitting InP quantum dots with a photoluminescence quantum yield greater than 80% can usually be obtained by constructing core–shell or alloy-type quantum dots,[8,9] the corresponding QLED still exhibits poor EQE (2.8%).[10] This indicates the EQE of InP QLED is determined by the combined effect of multiple factors. One of them is that QDs embedded in QLED architectures are susceptible to spectral diffusion under external electric fields, primarily as a consequence of the quantum-confined Stark effect (QCSE). Furthermore, the spectral diffusion may affect the rate of radiation combination as well as EQE.

Experimental studies have documented field-induced emission phenomena in InP QDs. For example, Suh *et al.*[11] observed a significant redshift and broadening in the electroluminescence spectra of blue InP QLEDs compared to photoluminescence spectra, while Yu *et al.* reported a maximum redshift of 19 nm (from 465 to 484 nm).[12] This electric-field-induced spectral modulation, often termed the Stark effect, is

College of Physics and Electronic Engineering, Northwest Normal University, Lanzhou 730070, China. E-mail: duning@nwnu.edu.cn

© 2025 The Author(s). Published by the Royal Society of Chemistry

Open Access Article. Published on 12 November 2025. Downloaded on 12/24/2025 5:45:51 PM. This article is licensed under a Creative Commons Attribution-NonCommercial 3.0 Unported Licence.

attributed to alterations in the band-edge energy landscape and reduction in effective bandgap.[13] In contrast, a recent study by Daibagya[14] found no observable Stark shift in the photoluminescence spectra of CdTe/SiO_2 QDs with a mean radius of 1.74 nm, attributing this to strong spatial confinement that suppresses field-induced dipole formation. Further investigations have revealed material and structure-dependent variations in the QCSE. Usman[15] studied $GaBi_xAs_{1-x}$/GaAs quantum wells, showing that at a low Bi content ($x = 3.125\%$), the Stark shift is unconventional due to strong localization of hole states caused by the presence of Bi clusters, while at higher Bi concentrations, a conventional quadratic dependence on the electric field emerges, regardless of field direction, similar to traditional III–V materials. Field polarity can also produce asymmetric spectral responses; for example, blue shifts are observed under fields opposing the intrinsic dipole direction.[16] Additionally, Heyn *et al.*[17] highlighted that the geometry of QDs, such as cones *versus* symmetric dots, significantly influences both the magnitude and symmetry of the Stark shift, correlating with the electron–hole spatial separation in the absence of an applied field.

The complex behavior of field-induced spectral shifts in QDs is commonly interpreted through contributions from both permanent dipole moments and linear polarizability. The direction and magnitude of the shift—red or blue—depend on the interplay between these two factors, with permanent dipole moments enabling bidirectional shifts and polarizability causing exclusively red shifts. Such dependencies have been exploited in several studies to extract exciton dipole moments and polarizabilities by fitting the quadratic relation between the Stark energy shift and applied field strength.[18–23]

Encapsulation of QDs in core–shell architectures has been shown to mitigate surface defect states and enhance fluorescence quantum yield.[24] This work systematically explores how external electric fields modulate the fluorescence response, with a focus on the field-induced Stark effect within InP/ZnSe core/shell engineered nanostructures.

2 Calculation methods

In this work, a nearly spherical indium phosphide nanocrystal, denoted as $(InP)_{77}$ with an approximate diameter of 2.0 nm, was derived by isolating a cluster from the bulk cubic lattice structure.[25–27] This undoped nanocluster exhibits C_{3v} point group symmetry. To generate core/shell architectures, the outer indium atoms on the InP cluster were selectively replaced with zinc, while phosphorus atoms were substituted with selenium, yielding two distinct configurations: $(InP)_{10}(ZnSe)_{67}$, representing a smaller core, and $(InP)_{27}(ZnSe)_{50}$, representing a large core. To eliminate unsatisfied surface bonds, pseudo-hydrogen atoms with fractional charges were used for surface passivation. These pseudo-atoms were assigned effective nuclear charges tailored to compensate for the valence of the surface atoms, following the electron counting principle, where the fractional charge is given by $(8 - Z)/4$ and Z represents the valence electron count of the surface species.[28] In this work, the passivating pseudo-hydrogen bonded to surface In, Zn, P, and Se were set to assigned nuclear charges of 1.25, 1.50, 0.75, and 0.50, respectively, maintaining the system's overall charge neutrality.

All model geometries were fully relaxed in their electronic ground states using density functional theory (DFT) as implemented in the Gaussian 16 software.[29] The PBE0 hybrid exchange-correlation functional[30] was selected for its demonstrated accuracy in modeling the structural and electronic features of indium phosphide nanomaterials.[25,31,32] Atomic orbitals for each element were described using the LanL2DZ effective core potential basis set.[33,34] SCF cycles and geometry optimizations were achieved using the default convergence criteria of the Gaussian 16 software:10^{-8} hartree for the self-consistent field convergence, maximum force of 0.000450 hartree/bohr, RMS force of 0.000300 hartree/bohr, maximum displacement of 0.001800 bohr, and RMS displacement of 0.001200 bohr. Structural analysis revealed that the optimized $(InP)_{77}$-G and $(InP)_{10}(ZnSe)_{67}$-G exhibit C_{3v}, whereas $(InP)_{27}(ZnSe)_{50}$-G adopts C_s symmetry in its relaxed configuration (see Fig. 1).

Following the electron excitation, each nanostructure undergoes rapid geometry relaxation, reaching a new equilibrium on the picosecond timescale. According to Kasha's rule, fast internal conversion between higher excited states and the lowest singlet (S_1) state ensures that fluorescence emission is governed by the $S_1 \rightarrow S_0'$ transition.[35] This electron transition model is clearly illustrated in Fig. S1 of the SI. Therefore, the influence of the electric field-induced Stark shifts was examined using the S_1-relaxed geometries. The energy gap between S_1 and S_0' directly yields the emission energy ΔE. The same computational approach, including functionals, pseudopotentials, and basis sets, was employed in the time-dependent DFT (TDDFT) calculations for optimizing S_1 geometries. The lowest singlet excited-state structures of $(InP)_{77}$-E, $(InP)_{10}(ZnSe)_{67}$-E, and $(InP)_{27}(ZnSe)_{50}$-E are given in Fig. 1. The corresponding atom coordinates are listed at the end of the SI. Since the cluster models are derived from the bulk cubic lattice structure and have an approximate diameter of 2.0 nm, the structural distortion after being excited was not significant, but only a decrease in symmetry (C_s or C_1). We use the root mean square displacement to measure the difference between the ground and excited state geometries.

$$\mathrm{RMSD} = \sqrt{\frac{1}{N}\sum_i \left[(x_i - x_i')^2 + (y_i - y_i')^2 + (z_i - z_i')^2 \right]} \quad (1)$$

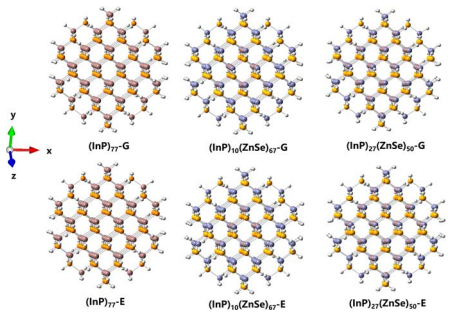

Fig. 1 Optimized ground-state (-G) and the lowest singlet excited-state (-E) geometries of $(InP)_{77}$, $(InP)_{10}(ZnSe)_{67}$, and $(InP)_{27}(ZnSe)_{50}$.

© 2025 The Author(s). Published by the Royal Society of Chemistry

Open Access Article. Published on 12 November 2025. Downloaded on 12/24/2025 5:45:51 PM. This article is licensed under a Creative Commons Attribution-NonCommercial 3.0 Unported Licence.

where x_i, y_i, and z_i are the coordinates of i-th atom in the S_0 structure, and $x_i^{'}$, $y_i^{'}$ and $z_i^{'}$ are the coordinates of i-th atom in the S_1 structure. Computed RMSD values are 0.034 Å for $(InP)_{77}$, 0.090 Å for $(InP)_{10}$ $(ZnSe)_{67}$ and 0.042 Å for $(InP)_{27}$ $(ZnSe)_{50}$. Therefore, it is difficult to observe clear changes through static graphics.

The influence of external electric fields on these systems was probed by introducing a "field" keyword during calculations. The field's magnitude and direction were controlled by the parameter $M \pm N$, where M indicates multipolarity and $N\times0.0001$ specifies the field strength in atomic units (a.u.). For instance, specifying "Field = $z + N$" applies a field from the positive z-direction to the negative z-direction, while "Field = $z - N$" orients it oppositely. In this work, the fields along the x,y, and z-axes were incremented from −0.0010 to +0.0010 a.u. in steps of 0.0002 a.u.(1 a.u. = 5.14×10^{11} V m^{-1}),[36] such as ±0.0002, ±0.0004, ±0.0006, ±0.0008 a.u….

The total energy of the system under an applied electric field was expanded as a Taylor series[37,38]

$$E(F) = E(0) + \left.\frac{\partial E}{\partial F}\right|_{F=0} F + \frac{1}{2}\left.\frac{\partial^2 E}{\partial F^2}\right|_{F=0} F^2 + \frac{1}{6}\left.\frac{\partial^3 E}{\partial F^3}\right|_{F=0} F^3 + \frac{1}{24}\left.\frac{\partial^4 E}{\partial F^4}\right|_{F=0} F^4 + \ldots = E(0) - \mu_0 F - \frac{1}{2}\alpha F^2 - \frac{1}{6}\beta F^3 - \frac{1}{24}\gamma F^4 \ldots \quad (2)$$

and

$$\mu_0 = -\left.\frac{\partial E}{\partial F}\right|_{F=0} \quad \alpha = -\left.\frac{\partial^2 E}{\partial F^2}\right|_{F=0} \quad \beta = -\left.\frac{\partial^3 E}{\partial F^3}\right|_{F=0} \quad \gamma = -\left.\frac{\partial^4 E}{\partial F^4}\right|_{F=0} \quad (3)$$

Here, μ_0 is the permanent dipole moment vector of the molecule at zero field. α is the static polarizability (second-rank tensor) and β is the first hyperpolarizability (third-rank tensor), representing linear and nonlinear optical response coefficients, respectively. γ is the second hyperpolarizability (fourth-rank tensor).

3 Results and discussion

3.1 Energy profiles of ground and excited states in applied electric fields

As outlined in computational methodology, the total energy of each nanostructure subjected to an electric field can be represented as a Taylor expansion. Table 1 summarizes the permanent dipole moments μ_{0i} and static polarizabilities α_{ii} calculated by Gaussian 16 for both ground and excited states of $(InP)_{77}$-E, $(InP)_{10}(ZnSe)_{67}$-E, and $(InP)_{27}(ZnSe)_{50}$-E, corresponding to the linear and quadratic terms in the expansion. Substituting these values into the truncated Taylor series (excluding higher-order terms), analytic expressions for the energies in $S_0^{'}$-state and S_1-state were derived for fields oriented along the x, y, and z axes. The explicit forms of these equations are provided in SI (eqn S1–S18). Meanwhile, the computed DFT energies of both electronic states and differences are listed in Tables S1–S3 (see SI).

In Fig. 2, the computed DFT energies (symbols) are compared to the values generated from the analytic equations (curves), showing excellent agreement and a predominantly quadratic relationship between the energy and the magnitude of the applied field. The most special one is the energy of $S_0^{'}$ in $(InP)_{10}(ZnSe)_{67}$-E when the electronic field is applied in the z-axis. Within the range of the applied electric field, no inflection point of the parabola was observed, presenting a linear-like characteristic. This is because the absolute value of the permanent dipole moment μ_{0i} of $S_0^{'}$-state is up to 3.9311 a.u., resulting in the linear term gaining more dominance.

3.2 Stark modulation of fluorescence emission energy

The fluorescence emission energy (ΔE), defined as the energy difference between the S_1 and $S_0^{'}$-states, is directly influenced by the presence of an external electric field. ΔE under various field conditions is computed as described by eqn (4)–(6), incorporating the excitation-induced changes in permanent dipole moment and polarizability.[21,39–42] Changes in the dipole moment upon excitation $\Delta\mu_{0i}$ result in a linear field dependence of the transition energy, while modifications in polarizability $\Delta\alpha_{ii}$ yield a quadratic response.

$$\Delta E(F_x) = E^{S_1}(F_x) - E^{S_0^{'}}(F_x) = E^{S_1}(0) - E^{S_0^{'}}(0) - \left(\mu_{0x}{}^{S_1} - \mu_{0x}{}^{S_0^{'}}\right) \times F_x - \frac{1}{2} \times \left(\alpha_{xx}{}^{S_1} - \alpha_{xx}{}^{S_0^{'}}\right) \times F_x{}^2 = \Delta E(0) - \Delta\mu_{0x} \times F_x - \frac{1}{2} \times \Delta\alpha_{xx} \times F_x{}^2 \quad (4)$$

similarly

$$\Delta E(F_y) = E^{S_0}(F_y) - E^{S_0^{'}}(F_y) = \Delta E(0) - \Delta\mu_{0y} \times F_y - \frac{1}{2} \times \Delta\alpha_{yy} \times F_y{}^2 \quad (5)$$

$$\Delta E(F_z) = E^{S_1}(F_z) - E^{S_0^{'}}(F_z) = \Delta E(0) - \Delta\mu_{0z} \times F_z - \frac{1}{2} \times \Delta\alpha_{zz} \times F_z{}^2 \quad (6)$$

As depicted in Fig. 3, the emission energy ΔE, as obtained from the analytical approach, agrees well with the numerical DFT results under varying electric field orientations. For $(InP)_{77}$ quantum dots, the ΔE shows a clear parabolic response to the field applied in the x direction, peaking when the field is absent. This pattern means the spectral peak consistently shifts to lower energies, no matter the direction of the field. Along the y and z axes, however, the response is more complex, combining both linear and nonlinear behaviors. When the field is aligned with the z axis, the energy shift curve becomes asymmetric, and a slight shift to higher energy is observed at stronger positive fields. Along y, larger changes in the dipole (1.3663 a.u.) result

Open Access Article. Published on 12 November 2025. Downloaded on 12/24/2025 5:45:51 PM.
This article is licensed under a Creative Commons Attribution-NonCommercial 3.0 Unported Licence.

Table 1 The permanent dipole moment μ_{0i} (unit: a.u.), static polarizability α_{ii} (unit: a.u.) of S_0'-state and S_1-state, as well as the difference between these two states, and the percentage contribution of orbital transitions HOMO → LUMO to the electron excitation

$(InP)_{77}$-E	μ_{0x}	μ_{0y}	μ_{0z}	α_{xx}	α_{yy}	α_{zz}	H → L
S_0'	0.0000	−0.7011	−0.0391	4633.448	4657.133	4185.229	
S_1	0.0000	0.6652	−0.2145	5610.170	5648.681	4754.469	
S_1–S_0'	0.0000	1.3663	−0.1754	976.722	991.548	569.240	96.16%
$(InP)_{10}(ZnSe)_{67}$-E	μ_{0x}	μ_{0y}	μ_{0z}	α_{xx}	α_{yy}	α_{zz}	H → L
S_0'	−0.0015	−0.5701	−3.9311	3915.272	3943.479	3622.894	
S_1	0.0008	0.2025	−1.1009	4590.244	4625.135	3860.934	
S_1–S_0'	0.0023	0.7726	2.8302	674.972	681.656	238.040	98.28%
$(InP)_{27}(ZnSe)_{50}$-E	μ_{0x}	μ_{0y}	μ_{0z}	α_{xx}	α_{yy}	α_{zz}	H → L
S_0'	0.0000	0.4083	1.0647	4171.188	4200.880	3785.502	
S_1	0.0000	−1.2451	0.8296	5408.003	5129.216	4219.542	
S_1–S_0'	0.0000	−1.6534	−0.2351	1236.814	928.636	434.040	97.41%

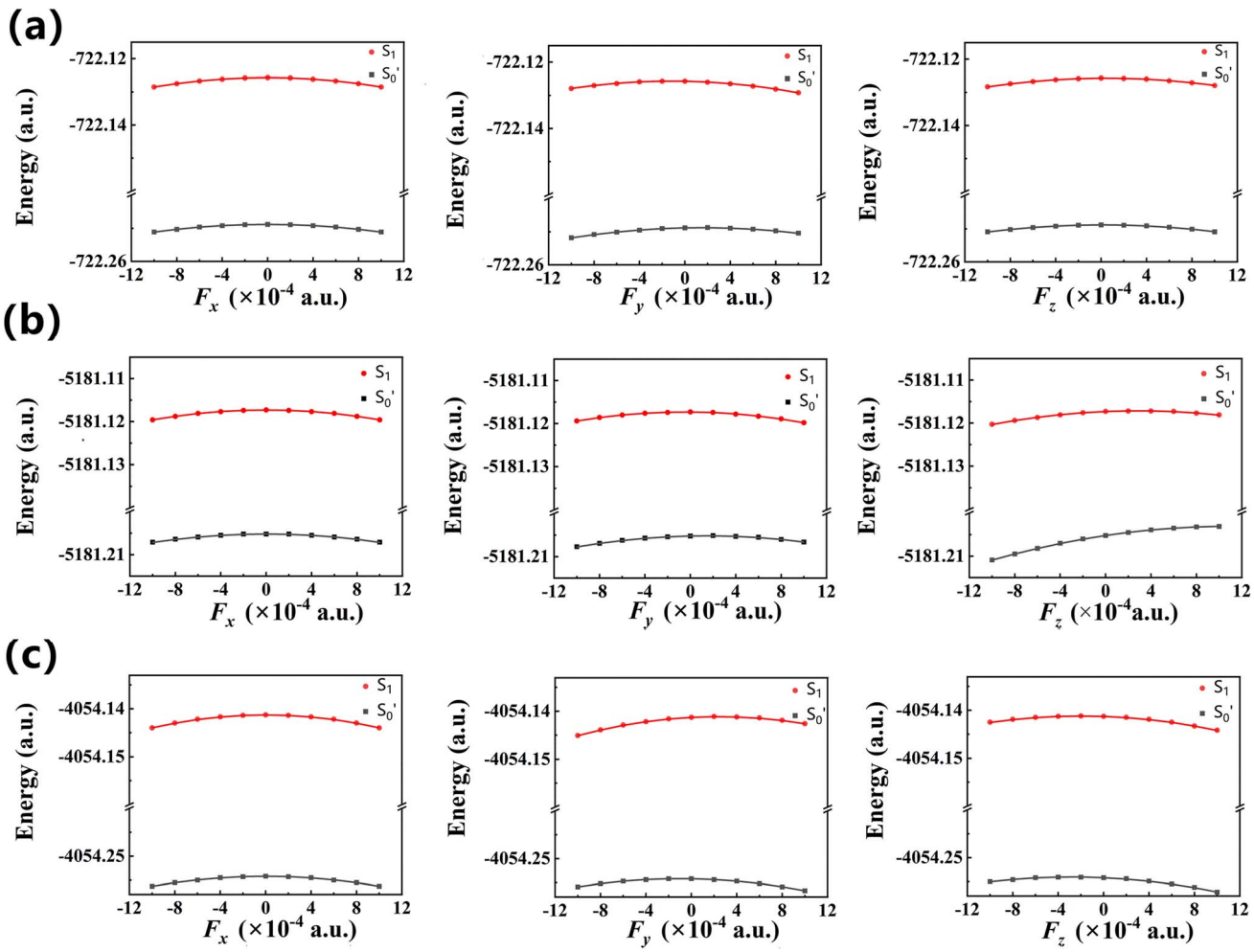

Fig. 2 Ground-state (S_0') and excited-state (S_1) energies for (a) $(InP)_{77}$-E, (b) $(InP)_{10}(ZnSe)_{67}$-E, and (c) $(InP)_{27}(ZnSe)_{50}$-E as a function of electric field strength. Black and red symbols denote DFT data for *x*, *y*, and *z* field orientations; corresponding curves are obtained from analytic energy models (eqn (S1)–(S18)).

© 2025 The Author(s). Published by the Royal Society of Chemistry

Open Access Article. Published on 12 November 2025. Downloaded on 12/24/2025 5:45:51 PM.
This article is licensed under a Creative Commons Attribution-NonCommercial 3.0 Unported Licence.

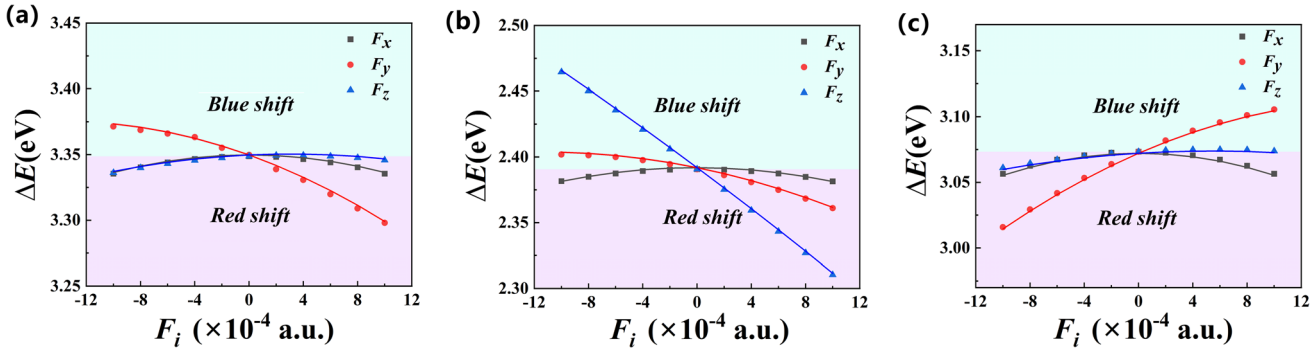

Fig. 3 Field-dependent emission energy ΔE for (a) $(InP)_{77}$-E, (b) $(InP)_{10}(ZnSe)_{67}$-E, and (c) $(InP)_{27}(ZnSe)_{50}$-E. Calculated data points (black, red, blue) indicate DFT results for electric fields applied along x, y, and z axes, respectively. The corresponding colored curves show theoretical fits based on the analytic eqn (4)–(6). The date above the boundary line indicates a blue shift, while the area below it indicates a red shift.

in an even more pronounced blue shift, with the parabola's symmetry notably offset. These observations demonstrate that, despite homogeneousness, the field response of InP QDs can be strongly directional, which is consistent with prior reports for other types of nanocrystals, such as CdSe, where field alignment and nanocrystal orientation both significantly influence the Stark effect.[43]

For $(InP)_{10}(ZnSe)_{67}$ QDs, core/shell nanocrystals, the field-induced emission energy variation is mainly quadratic in the x direction, but shows a strong linear shift along z, resulting in red or blue shifts depending on the field orientation. With the field along y, both quadratic and linear tendencies appear, leading to an asymmetric curve, though the overall magnitude of shift is less than in the linear-dominated case.

For $(InP)_{27}(ZnSe)_{50}$ (Fig. 3c), the shift follows a broadly similar pattern to $(InP)_{77}$ across all three field directions. Overall, these comparisons indicate that the observed field sensitivity of the fluorescence spectrum depends not only on the direction of the applied field, but also on the internal structure and core thickness of the quantum dots. Adjusting the core size or composition can thus serve as a practical way to tune Stark shifts in engineered QD systems.

3.3 Spatial separation of electrons and holes in core/shell quantum dots

The nature of the Stark effect in fluorescence emission is dictated by the behavior of the dipole moment change upon excitation. When this change is close to zero, the Stark shift follows a purely quadratic trend; when it is large, a predominantly linear dependence appears, while most cases exhibit a blend of both characteristics. This dipole change is fundamentally linked to the spatial redistribution of positive and negative charges after exciton formation. Specifically, it reflects the intrinsic dipole moment of the exciton p_{0i}, proportional to the average electron–hole distance at zero field (D_{0i}, where $i = x, y, z$), as expressed by $p_{0i} = qD_{0i}$, with q as the elementary charge.[19,44,45] The centroid-based electron–hole separation D_i, where $i = x, y, z$, can be defined as the difference between the mean positions of electrons ($X/Y/Z_e$) and holes ($X/Y/Z_h$):

$$D_x = X_h - X_e = \int x\rho_h(r)dr - \int x\rho_e(r)dr \quad (7\text{-}1)$$

$$D_y = Y_h - Y_e = \int y\rho_h(r)dr - \int y\rho_e(r)dr \quad (7\text{-}2)$$

$$D_z = Z_h - Z_e = \int z\rho_h(r)dr - \int z\rho_e(r)dr \quad (7\text{-}3)$$

where ρ_h and ρ_e denote the spatial distributions of holes and electrons in the excited state.[46] Although the electronic transitions are strictly changes in quantum states, they are often more intuitively understood *via* orbital transitions: excitation is commonly described as the promotion of an electron from an occupied to an unoccupied orbital. In InP-based quantum dots, the $S_0' \rightarrow S_1$ excitation is dominated by a HOMO → LUMO transition, accounting for around 95% (listed in Table 1) of the transition character. Fig. 4 displays the spatial distribution of electrons and holes, as well as the relevant molecular orbitals at zero field, generated with Multiwfn.[47,48] The close similarity between the electron/hole and orbital distributions supports this simplified model, with additional perspectives available in SI (see Fig. S2 and S3).

Using eqn (7), the computed initial electron–hole spatial separations D_{0i} (in Å) at zero field are obtained: 0.000 (x), 2.477 (y), −0.383 (z) for $(InP)_{77}$; 0.004, 1.179, 4.213 for $(InP)_{10}(ZnSe)_{67}$; 0.000, −2.700, −0.365 for $(InP)_{27}(ZnSe)_{50}$. These correspond to the intrinsic exciton dipole moment p_{0i} (in a.u.): 0.000 (x), 4.502 (y), −0.696 (z) for $(InP)_{77}$; 0.007, 2.190, 7.832 for $(InP)_{10}(ZnSe)_{67}$; 0.000, −4.972, −0.671 for $(InP)_{27}(ZnSe)_{50}$. By comparison, changes of dipole moment $\Delta\mu_{0i}$ fitted *via* Stark shift analysis (see Table 1) are smaller, highlighting the fact that centroid-based separation (carried out by Multiwfn) uses unrelaxed excited-state densities, essentially an instantaneous snapshot after excitation, whereas Stark-fit values reflect post-relaxation densities, thus providing a more accurate physical representation. This distinction explains why direct experimental determination of electron–hole separation is often challenging, and why many studies rely on Stark effect measurements to infer dipole characteristics.

Under applied electric fields, the separation between electrons and holes is dynamically modulated: the field can either stretch or compress this distance, as summarized in Tables S4–S6 (see SI). Fig. 5 presents how the emission energy ΔE (left axis)

Open Access Article. Published on 12 November 2025. Downloaded on 12/24/2025 5:45:51 PM.
This article is licensed under a Creative Commons Attribution-NonCommercial 3.0 Unported Licence.

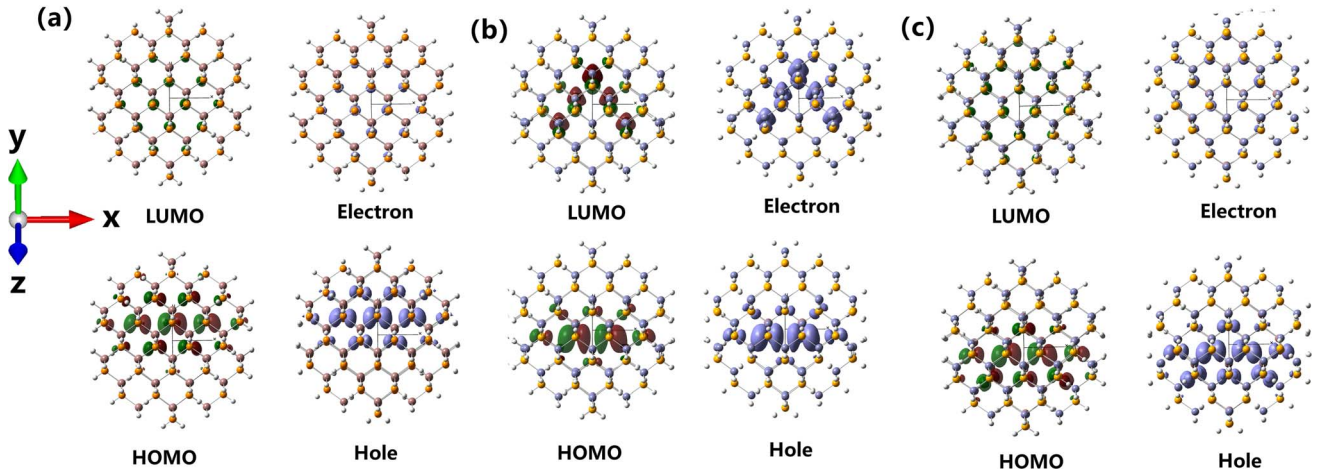

Fig. 4 Electron and hole spatial distributions, HOMO, and LUMO at zero field of (a) $(InP)_{77}$-E, (b) $(InP)_{10}(ZnSe)_{67}$-E and (c) $(InP)_{27}(ZnSe)_{50}$-E.

and electron–hole separation D_i (right axis) evolve with field strength. Notably, ΔE changes in a quadratic or linear function with the field, while D_i changes linearly. There is a clear anti-correlation: as $|D_i|$ decreases, ΔE increases and reaches a maximum near $|D_i| = 0$. This pattern matches findings from studies on geometry-dependent Stark effects in other nanostructures, such as GaAs quantum dots.[17] In these, systems with zero initial electron–hole offset exhibit symmetric (parabolic) Stark responses, while those with pre-existing charge separation display asymmetric shifts. To more clearly demonstrate the influence of the electric field on dipole alignment, Fig. 6 presents the distribution of electrons and holes under

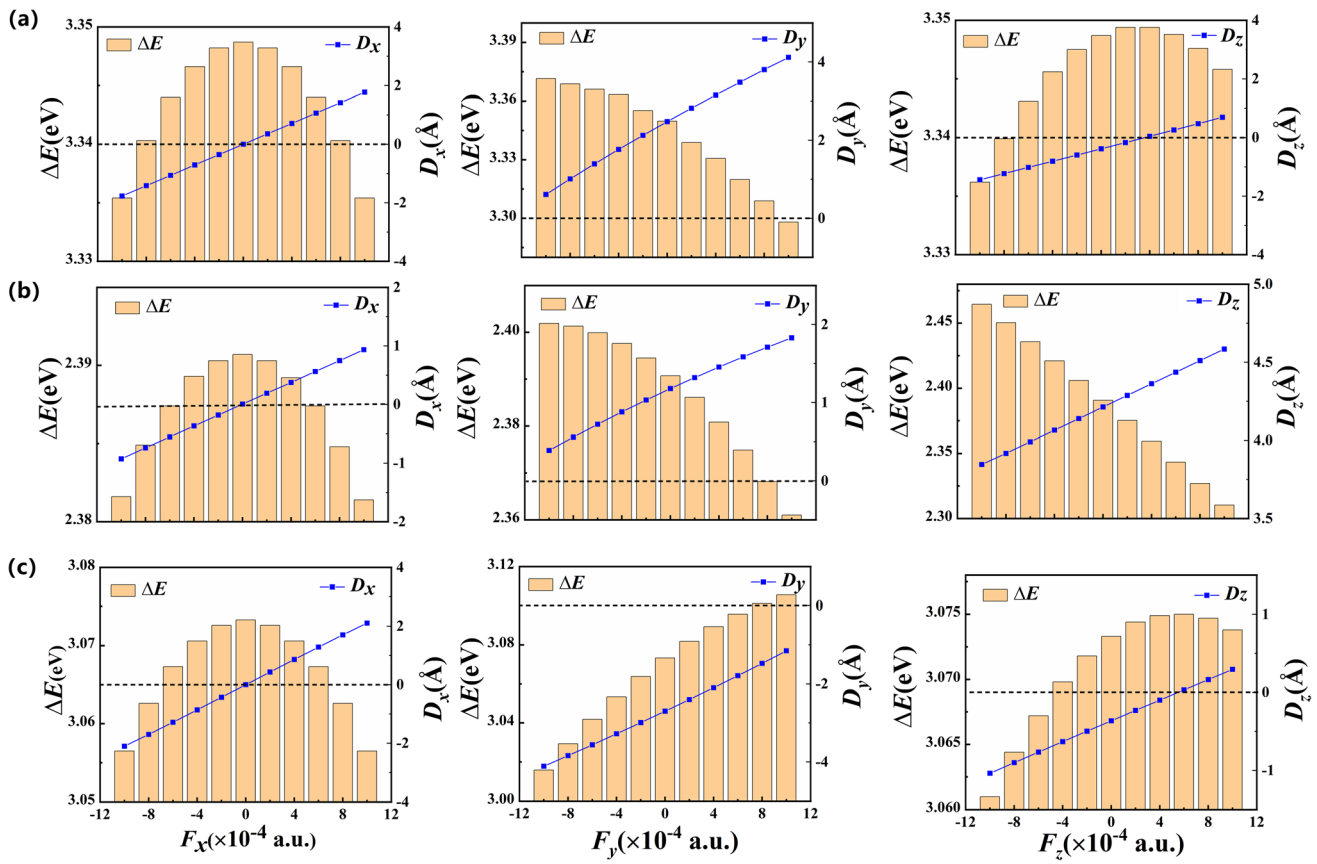

Fig. 5 Relationship between emission energy (ΔE, left Y-axis) and electron–hole separation (D_i for x, y, z; right axis) in (a) $(InP)_{77}$-E, (b) $(InP)_{10}(ZnSe)_{67}$-E and (c) $(InP)_{27}(ZnSe)_{50}$-E.

© 2025 The Author(s). Published by the Royal Society of Chemistry

Open Access Article. Published on 12 November 2025. Downloaded on 12/24/2025 5:45:51 PM.
This article is licensed under a Creative Commons Attribution-NonCommercial 3.0 Unported Licence.

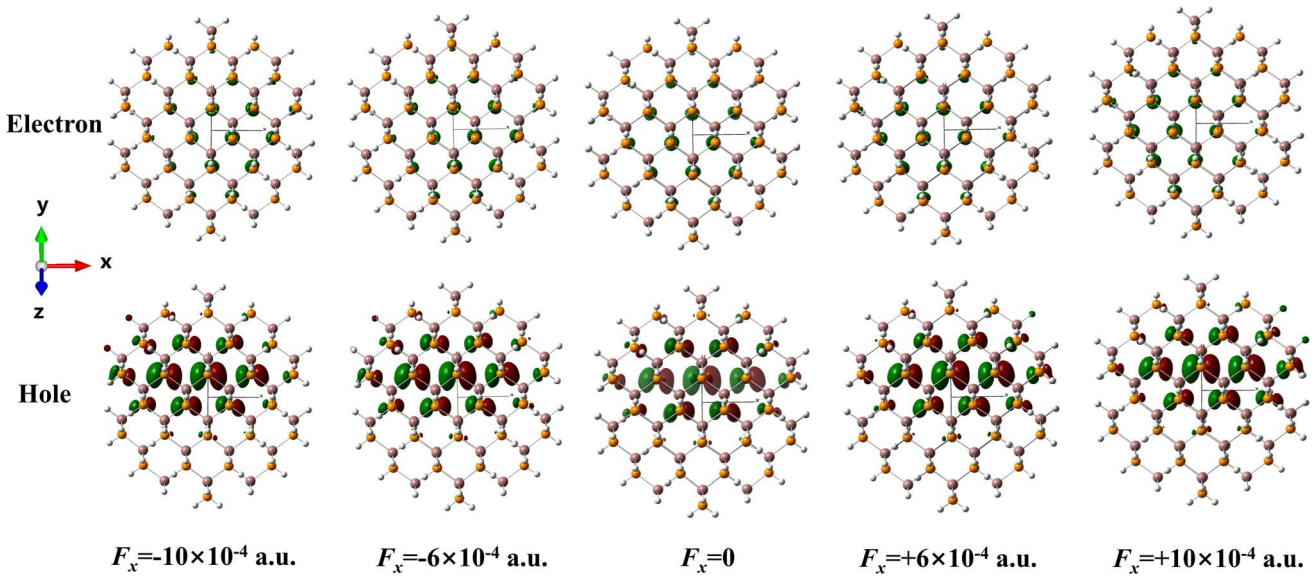

Fig. 6 Distribution of holes and electrons under various electronic fields in the *x*-axis for $(InP)_{77}$-E. A vivid diagram that presents the interaction between the electric field and the dipole aligns is given in Fig. S6 of the SI. For all studied QDs, the initial *x*-direction electron–hole separation is negligible, so an electric field in this axis always increases $|D_x|$, resulting in a consistent red shift. Along *y* and *z*, larger separations exist at zero field. If the external field aligns with D_{0i}, the electron and hole are pulled further apart (red shift); if opposed, the two are pushed together, potentially producing a blue shift. This blue shift ceases once the separation reaches zero, after which further field application increases $|D_i|$ again, restoring the red shift. Overall, these data clearly demonstrate the inverse relationship between emission energy and spatial charge separation, consistent with earlier experimental observations.[49–51]

various electric fields in the *x*-axis for $(InP)_{77}$. The results of the other two structures belonging to the *x* and *y* directions, respectively, are depicted in Fig. S4 and S5 of the SI. Although the differences are subtle, a careful comparison still reveals that the applied fields do not affect the symmetry of the holes and electrons, but just slightly shift the distribution of the electrons and holes (the holes move along the direction of the electric field, while the electrons move in the opposite direction of the electric field).

Fig. 5b shows that for $(InP)_{10}(ZnSe)_{67}$, ΔE exhibits a linear dependence on the *z*-oriented electric field. This occurs because $|D_{0z}|$ is already large (4.213 Å) at zero field, so the field range used cannot reduce the electron–hole distance to zero or create a ΔE maximum. This substantial separation stems from the intrinsic electronic arrangement of the core/shell structure. Fig. 7 illustrates the total and core-projected density of states for $(InP)_{77}$, $(InP)_{10}(ZnSe)_{67}$, and $(InP)_{27}(ZnSe)_{50}$ QDs. In the pure $(InP)_{77}$, two projected density distributions were made, corresponding to the $(InP)_{10}$ (blue line) and $(InP)_{27}$ (red line) at the core, respectively. Although the composition of the core atoms was set to be uniform, the InP/ZnSe core/shell structure shows a greater contribution of the core to the HOMO and LUMO levels than pure InP. This is because the pure $(InP)_{77}$ can be regarded as the type I energy band structure with the shell layer removed.[51] The composition of its HOMO and LUMO does not show any significant localization but exhibits something related to the number of atoms.

InP, which forms the core, has a narrower band gap than ZnSe, resulting in higher-lying HOMO and lower-lying LUMO relative to the shell. As a result, InP/ZnSe quantum dots

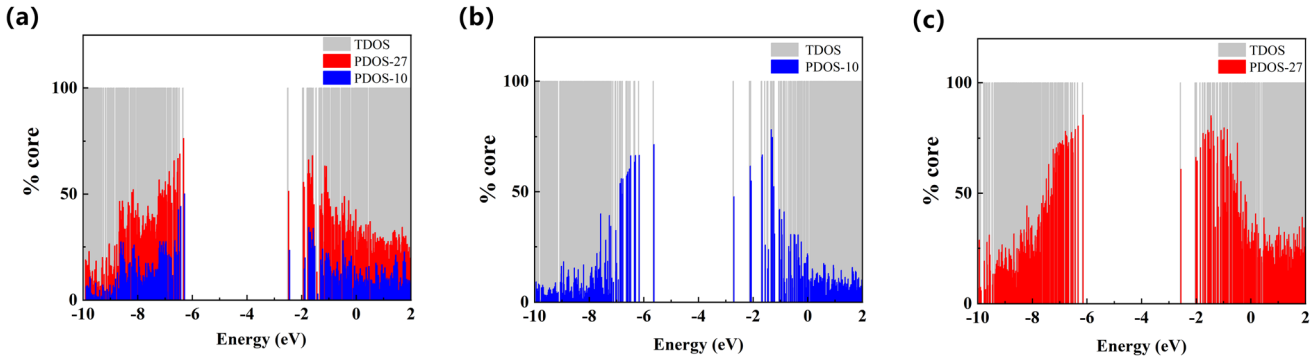

Fig. 7 Total and core-projected density of states for (a) $(InP)_{77}$-E, (b) $(InP)_{10}(ZnSe)_{67}$-E, and (c) $(InP)_{27}(ZnSe)_{50}$-E.

Open Access Article. Published on 12 November 2025. Downloaded on 12/24/2025 5:45:51 PM. This article is licensed under a Creative Commons Attribution-NonCommercial 3.0 Unported Licence.

generally display a type-I band alignment, confining both electrons and holes to the core region.[52–54] However, in $(InP)_{10}(ZnSe)_{67}$, the HOMO remains predominantly localized in the core (~70%), while the LUMO is delocalized between the core and shell (48% core, 52% shell), indicating a hybridized state. This finding is corroborated by orbital distributions in Fig. 4 and aligns with previous observations that energy level proximity between core and shell leads to hybridization.[55] The minimal LUMO offset in $(InP)_{10}(ZnSe)_{67}$ QDs gives rise to characteristics similar to quasi-type-II nanostructures, such as CdSe/CdS with small cores.[56] In contrast, both frontier orbitals in $(InP)_{27}(ZnSe)_{50}$, are strongly core-localized (85% HOMO, 60% LUMO), typical of type-I alignment. Recent works confirm that shrinking InP core size[57] or expanding the ZnS shell thickness[58] decreases the band offset between core and shell. In larger quantum dots, the energy band distribution of the core and shell material is closer to that of the bulk material, so the energy level distribution may be closer to the assumed situation (as shown in Fig. S7), and thus the localized states will also exist.

In addition, the atomic composition of the density of states is also given in Fig. S8 of the SI. In pure $(InP)_{77}$, the occupied orbitals (valence band) are mainly contributed by P atoms, while the unoccupied orbitals (conduction band) are more dominated by In. Upon the addition of the ZnSe shell to the InP system (going from $(InP)_{77}$ to $(InP)_{10}(ZnSe)_{67}$ and $(InP)_{27}(ZnSe)_{50}$), the bandgap for the system decreases (by 0.92 eV and 0.26 eV), as anticipated due to the ability for the wavefunction to diffuse into the shell. Examination of the density of states plot for the $(InP)_{10}(ZnSe)_{67}$ structure shows that the partial density of states of In atoms and P atoms is significantly lower than that of Zn atoms and Se atoms due to the difference in the number of atoms. The occupied orbitals are mainly contributed to by Se atoms, except that the HOMO is derived from P. The unoccupied orbitals are more dominated by Zn. In $(InP)_{27}(ZnSe)_{50}$, the partial density of states of In atoms and P atoms have risen than those in $(InP)_{10}(ZnSe)_{67}$. The occupied orbitals are also mainly contributed to by Se atoms and P atoms, except that the HOMO is derived from P. The unoccupied orbitals are more dominated by Zn and In. The above results are essentially consistent with the results of the core/shell project density of states.

The partial band delocalization in $(InP)_{10}(ZnSe)_{67}$ favors electron–hole separation under an applied field. Depending on the field direction, this can push charge carriers toward or away from the interface, resulting in blue or red shifts in the emission spectrum, respectively. Behavior reminiscent of the quantum-confined Stark effect (QCSE) observed in other colloidal quantum dots and nanorods.[51] Typically, type-I structures show a parabolic (quadratic) response to field strength, while type-II systems tend to exhibit a more linear dependence.

According to experimental studies, Mei *et al.*[10] found a redshift of 10 nm in electroluminescence compared to photoluminescence in blue pure InP quantum dots, which belong to the Type I band structure. Suh *et al.*[11] also observed a significant redshift and broadening in the electroluminescence spectra of blue InP/ZnS QLEDs. The core and shell sizes of the samples used in the experiment are 1.80 nm and 4.95 nm. In addition, Yu *et al.* reported a maximum redshift of 19 nm (from 465 to 484 nm)[12] in a blue InP/ZnS QLED. The InP core and ZnS shell sizes of the samples used in the experiment are 2.50 nm and 4.80 nm. Due to the differences in the shell material, we cannot directly determine which type of band distribution the above two InP/ZnS QDs belong to. However, regardless of the type of energy band structure it belongs to, the spectrum generally undergoes a redshift in most cases when an electric field is applied (see Fig. 3), unless the direction and magnitude of the applied electric field are strictly controlled. This is in correspondence with the redshift phenomenon observed in the above three experiments.

4 Conclusions

First-principles calculations were used to evaluate the Stark shifts of fluorescence spectra in InP core and InP/ZnSe core/shell quantum dots subjected to varying field strengths and orientations. Three classes of field-dependent spectral shifts: quadratic, linear, and mixed modes were revealed. Pure quadratic shifts arise when the dipole moment change upon excitation is negligible, while large dipole changes yield predominantly linear behavior. Intermediate cases display both effects.

The permanent exciton dipole, which depends on the intrinsic electron–hole separation at zero field, is central to understanding these effects. Analysis of excited-state densities provides quantitative insight: along the x axis, the electron–hole separation is negligible at zero field, so any applied field increases this distance and induces a red shift. Along y and z, initial separations are more substantial. A field aligned from electron to hole simplifies the distance (leading to a redshift), while an opposing field can reduce separation and cause blue shifts. Across all cases, the emission energy increases as the electron–hole separation decreases, with a maximum near zero separation.

The magnitude of intrinsic electron–hole separation is dictated by the quantum dot's electronic structure. In $(InP)_{10}(ZnSe)_{67}$, the small core and band structure promote quasi-type-II behavior with pronounced electron–hole separation, especially along z. For $(InP)_{27}(ZnSe)_{50}$, and pure $(InP)_{77}$, both charge carriers remain largely confined to the core, resembling type-I alignment. The calculations demonstrate that adjusting the thickness of the InP core and the ZnSe shell provides a route for tuning the magnitude and character of Stark shifts in InP/ZnSe quantum dots. In fact, the Stark effect of the fluorescence spectra can also influence the radiative lifetime of quantum dots as well as the efficiency of the device. This is a topic that needs to be explored in the future.

Author contributions

Ning Du: conceptualization; data curation; methodology; funding acquisition; and writing – original draft. Hongshan Chen: resources; supervision; and writing – review & editing.

© 2025 The Author(s). Published by the Royal Society of Chemistry

Open Access Article. Published on 12 November 2025. Downloaded on 12/24/2025 5:45:51 PM. This article is licensed under a Creative Commons Attribution-NonCommercial 3.0 Unported Licence.

Conflicts of interest

There are no conflicts of interest to declare.

Data availability

The data supporting this article are included within the main text or the supplementary information (SI). Supplementary information: explicit energy equations for fields oriented along the x, y, and z axes, schematic diagram of electron transition, electron and hole spatial distributions, electronic energy levels of selected III–V and II–VI semiconductors, total and atomic composition of the density of states, computed DFT energy of S_0'-state and S_1-state, electron–hole separation lengths, coordinates of all three structures. See DOI: **https://doi.org/10.1039/d5ra06323j**.

Acknowledgements

This work was supported by the National Natural Science Foundation of China (NSFC, Grant No. 12404464) and Northwest Normal University of China (NWNU-LKQN2022-06). The authors also appreciate Brandi M. Cossairt for offering the coordinate file of $(InP)_{77}$ cluster.

References

1 J. Song, O. Wang, H. Shen, Q. Lin, Z. Li, L. Wang, X. Zhang and L. S. Li, *Adv. Funct. Mater.*, 2019, **29**, 1808377.
2 Y. Deng, F. Peng, Y. Lu, X. Zhu, W. Jin, J. Qiu, J. Dong, Y. Hao, D. Di, Y. Gao, T. Sun, M. Zhang, F. Liu, L. Wang, L. Ying, F. Huang and Y. Jin, *Nat. Photonics*, 2022, **16**, 505–511.
3 G. Almeida, R. F. Ubbink, M. Stam, I. du Fossé and A. J. Houtepen, *Nat. Rev. Mater.*, 2023, **8**, 742–758.
4 Z. Cui, D. Yang, S. Qin, Z. Wen, H. He, S. Mei, W. Zhang, G. Xing, C. Liang and R. Guo, *Adv. Opt. Mater.*, 2023, **11**, 2202036.
5 H. Seo, J. H. Park, O. H. Kwon, O. P. Kwon, S. K. Kwak and S.-W. Kim, *Nanoscale Adv*, 2020, **2**, 5615–5622.
6 H. Li, Y. Bian, W. Zhang, Z. Wu, T. K. Ahn, H. Shen and Z. Du, *Adv. Funct. Mater.*, 2022, **32**, 2204529.
7 W.-C. Chao, T.-H. Chiang, Y.-C. Liu, Z.-X. Huang, C.-C. Liao, C.-H. Chu, C.-H. Wang, H.-W. Tseng, W.-Y. Hung and P.-T. Chou, *Comm. Mater.*, 2021, **2**, 96.
8 H. Zhang, X. Ma, Q. Lin, Z. Zeng, H. Wang, L. S. Li, H. Shen, Y. Jia and Z. Du, *J. Phys. Chem. Lett.*, 2020, **11**, 960–967.
9 K.-H. Kim, J.-H. Jo, D.-Y. Jo, C.-Y. Han, S.-Y. Yoon, Y. Kim, Y.-H. Kim, Y. H. Ko, S. W. Kim, C. Lee and H. Yang, *Chem. Mater.*, 2020, **32**, 3537–3544.
10 G. Mei, Y. Tan, J. Sun, D. Wu, T. Zhang, H. Liu, P. Liu, X. W. Sun, W. C. H. Choy and K. Wang, *Appl. Phys. Lett.*, 2022, **120**, 091101.
11 Y. H. Suh, S. Lee, S. M. Jung, S. Y. Bang, J. Yang, X. B. Fan, S. Zhan, C. Samarakoon, J. W. Jo, Y. Kim, H. W. Choi, L. G. Occhipinti, T. H. Lee, D. W. Shin and J. M. Kim, *Adv. Opt. Mater.*, 2022, **10**, 2102372.
12 P. Yu, Y. Shan, S. Cao, Y. Hu, Q. Li, R. Zeng, B. Zou, Y. Wang and J. Zhao, *ACS Energy Lett.*, 2021, **6**, 2697–2703.
13 J. P. A. de Jesus, M. Z. Jimenez and F. d. A. La Porta, *Comp. Mater. Sci.*, 2021, **188**, 110147.
14 D. S. Daibagya, S. A. Ambrozevich, I. A. Zakharchuk, A. V. Osadchenko, M. S. Smirnov, O. V. Ovchinnikov and A. S. Selyukov, *Opt. Mater.*, 2024, **150**, 115297.
15 M. Usman, *J. Phys. Condens. Matter.*, 2019, **31**, 415503.
16 B. Lv, T. Zhu, Y. Tang, Y. Lv, C. Zhang, X. Wang, D. Shu and M. Xiao, *Phys. Rev. Lett.*, 2021, **126**, 197403.
17 C. Heyn, L. Ranasinghe, M. Zocher and W. Hansen, *J. Phys. Chem. C*, 2020, **124**, 19809–19816.
18 D. Rana and A. Materny, *Spectrochim. Acta. A*, 2021, **253**, 119565.
19 J. D. Mar, J. J. Baumberg, X. L. Xu, A. C. Irvine and D. A. Williams, *Phys. Rev. B*, 2017, **95**, 201304.
20 L. Alaerts, Y. Xiong, S. Griffin and G. Hautier, *Phys. Rev. Mater.*, 2024, **8**, 106201.
21 J. Seufert, M. Obert, M. Scheibner, N. A. Gippius, G. Bacher, A. Forchel, T. Passow, K. Leonardi and D. Hommel, *Appl. Phys. Lett.*, 2001, **79**, 1033–1035.
22 L. Zhang, B. Lv, H. Yang, R. Xu, X. Wang, M. Xiao, Y. Cui and J. Zhang, *Nanoscale*, 2019, **11**, 12619–12625.
23 H. Huang, D. Csontosová, S. Manna, Y. Huo, R. Trotta, A. Rastelli and P. Klenovský, *Phys. Rev. B*, 2021, **104**, 165401.
24 E. Alexander, M. Kick, A. R. McIsaac and T. Van Voorhis, *Nano Lett.*, 2024, **24**, 7227–7235.
25 N. Park, F. W. Eagle, A. J. DeLarme, M. Monahan, T. LoCurto, R. Beck, X. Li and B. M. Cossairt, *J. Chem. Phys.*, 2021, **155**, 084701.
26 E. Cho, H. Jang, J. Lee and E. Jang, *Nanotechnology*, 2013, **24**, 215201.
27 E. Cho, T. Kim, S.-m. Choi, H. Jang, K. Min and E. Jang, *ACS Appl. Nano Mater.*, 2018, **1**, 7106–7114.
28 L.-W. Wang and J. Li, *Phys. Rev. B*, 2004, **69**, 153302.
29 M. J. Frisch, G. W. Trucks, H. B. Schlegel, G. E. Scuseria, M. A. Robb, J. R. Cheeseman, G. Scalmani, V. Barone, G. A. Petersson, H. Nakatsuji, X. Li, M. Caricato, A. V. Marenich, J. Bloino, B. G. Janesko, R. Gomperts, B. Mennucci, H. P. Hratchian, J. V. Ortiz, A. F. Izmaylov, J. L. Sonnenberg, D. Williams-Young, F. Ding, F. Lipparini, F. Egidi, J. Goings, B. Peng, A. Petrone, T. Henderson, D. Ranasinghe, V. G. Zakrzewski, J. Gao, N. Rega, G. Zheng, W. Liang, M. Hada, M. Ehara, K. Toyota, R. Fukuda, J. Hasegawa, M. Ishida, T. Nakajima, Y. Honda, O. Kitao, H. Nakai, T. Vreven, K. Throssell, J. A. Montgomery Jr, J. E. Peralta, F. Ogliaro, M. J. Bearpark, J. J. Heyd, E. N. Brothers, K. N. Kudin, V. N. Staroverov, T. A. Keith, R. Kobayashi, J. Normand, K. Raghavachari, A. P. Rendell, J. C. Burant, S. S. Iyengar, J. Tomasi, M. Cossi, J. M. Millam, M. Klene, C. Adamo, R. Cammi, J. W. Ochterski, R. L. Martin, K. Morokuma, O. Farkas, J. B. Foresman and D. J. Fox, *Gaussian 16 Rev. C.02*, Wallingford, CT, 2019.
30 C. Adamo and V. Barone, *J. Chem. Phys.*, 1999, **110**, 6158–6170.
31 P. T. Snee, *J. Phys. Chem. C*, 2021, **125**, 11765–11772.

Open Access Article. Published on 12 November 2025. Downloaded on 12/24/2025 5:45:51 PM.
This article is licensed under a Creative Commons Attribution-NonCommercial 3.0 Unported Licence.

32 A. Hassan, X. Zhang, C. Liu and P. T. Snee, *J. Phys. Chem. C*, 2018, **122**, 11145–11151.
33 P. J. Hay and W. R. Wadt, *J. Chem. Phys.*, 1985, **82**, 299–310.
34 W. R. Wadt and P. J. Hay, *J. Chem. Phys.*, 1985, **82**, 284–298.
35 M. E. Bathen, L. Vines and J. Coutinho, *J. Phys. Condens. Matter.*, 2020, **33**, 075502.
36 P. K. Bhattacharyya, *Comput. Theor. Chem.*, 2015, **1057**, 43–53.
37 D. M. Bishop, *Rev. Mod. Phys.*, 1990, **62**, 343–374.
38 D. Rayane, A. R. Allouche, E. Benichou, R. Antoine, M. Aubert-Frecon, P. Dugourd, M. Broyer, C. Ristori, F. Chandezon, B. A. Huber and C. Guet, *Eur. Phys. J. D*, 1999, **9**, 243–248.
39 F. C. Grozema, R. Telesca, H. T. Jonkman, L. D. A. Siebbeles and J. G. Snijders, *J. Chem. Phys.*, 2001, **115**, 10014–10021.
40 P. Kjellberg, Z. He and T. Pullerits, *J. Phys. Chem. B*, 2003, **107**, 13737–13742.
41 I. Zhigulin, J. Horder, V. Ivády, S. J. U. White, A. Gale, C. Li, C. J. Lobo, M. Toth, I. Aharonovich and M. Kianinia, *Phys. Rev. Appl.*, 2023, **19**, 044011.
42 Y. Xie, Y. Cui, L. Zhang and M. Yang, *J. Phys. Chem. C*, 2023, **127**, 2603–2611.
43 S. A. Empedocles and M. G. Bawendi, *Science*, 1997, **278**, 2114–2117.
44 T. Karin, X. Linpeng, M. M. Glazov, M. V. Durnev, E. L. Ivchenko, S. Harvey, A. K. Rai, A. Ludwig, A. D. Wieck and K.-M. C. Fu, *Phys. Rev. B*, 2016, **94**, 041201.
45 M. Sugisaki, H.-W. Ren, S. V. Nair, K. Nishi and Y. Masumoto, *Phys. Rev. B*, 2002, **66**, 235309.
46 X.-Y. Liu, Z.-W. Li, W.-H. Fang and G. Cui, *J. Phys. Chem. A*, 2020, **124**, 7388–7398.
47 T. Lu and F. Chen, *J. Comp. Chem.*, 2011, **33**, 580–592.
48 T. Lu, *J. Chem. Phys.*, 2024, **161**, 082503.
49 A. W. Achtstein, A. V. Prudnikau, M. V. Ermolenko, L. I. Gurinovich, S. V. Gaponenko, U. Woggon, A. V. Baranov, M. Y. Leonov, I. D. Rukhlenko, A. V. Fedorov and M. V. Artemyev, *ACS Nano*, 2014, **8**, 7678–7686.
50 J. Muller, J. M. Lupton, P. G. Lagoudakis, F. Schindler, R. Koeppe, A. L. Rogach, J. Feldmann, D. V. Talapin and H. Weller, *Nano Lett.*, 2005, **5**, 2044–2049.
51 K. Park, Z. Deutsch, J. J. Li, D. Oron and S. Weiss, *ACS Nano*, 2012, **6**, 10013–10023.
52 Q. Zheng, J. Wang, F. Huang, Z. Huang, S. Tian, Q. Chen, Y. Pei, K. Zheng and J. Tian, *ACS Energy Lett.*, 2024, **9**, 2358–2366.
53 S. Kim, J. Park, T. Kim, E. Jang, S. Jun, H. Jang, B. Kim and S. W. Kim, *Small*, 2010, **7**, 70–73.
54 P. Cavanaugh, X. Wang, M. J. Bautista, I. Jen-La Plante and D. F. Kelley, *J. Chem. Phys.*, 2023, **159**, 134704.
55 K. Jain, S. Kishor, K. S. Singh, M. Odelius and L. M. Ramaniah, *J. Phys. Chem. C*, 2021, **125**, 27046–27057.
56 D. Kong, Y. Jia, Y. Ren, Z. Xie, K. Wu and T. Lian, *J. Phys. Chem. C*, 2018, **122**, 14091–14098.
57 D. Respekta, P. Schiettecatte, L. Giordano, N. De Vlamynck, P. Geiregat, J. I. Climente and Z. Hens, *ACS Nano*, 2025, **19**, 19831–19840.
58 S. Savchenko, A. Vokhmintsev, M. Karabanalov, Y. Zhang, A. Henaish, A. Neogi and I. Weinstein, *Phys. Chem. Chem. Phys.*, 2024, **26**, 18727–18740.

© 2025 The Author(s). Published by the Royal Society of Chemistry